communications earth & environment

ARTICLE

https://doi.org/10.1038/s43247-022-00410-z OPEN

Patterns and frequency of projected future tropical cyclone genesis are governed by dynamic effects

Hiroyuki Murakami [1,2]✉ & Bin Wang[3,4]

Potential future changes in the genesis frequency and distribution of tropical cyclones are important for society, yet uncertain. Confidence in the model projections largely relies on whether we can physically explain why the models projected such changes. Here we analyze multi-model climate simulations, and find that future changes in the patterns and frequency of tropical cyclone genesis are largely governed by dynamic effects—that is, by human-induced changes in the atmospheric circulation. These large-scale circulation changes include decreases in the mid-level upward motion and lower-to-mid level cyclonic vorticity, and increases in vertical wind shear. Conversely, the thermodynamic effect—a result of increased maximum potential intensity in a warmer climate—would yield tropical cyclone genesis patterns that are opposite to the model projections. We conclude that dynamic changes in response to anthropogenic greenhouse gas emissions are an important factor in determining the response of tropical cyclones to global warming.

[1] University Corporation for Atmospheric Research, Boulder, CO, USA. [2] National Oceanic and Atmospheric Administration/Geophysical Fluid Dynamics Laboratory, Princeton, NJ, USA. [3] Department of Atmospheric Sciences and International Pacific Research Center, University of Hawaii at Manoa, Honolulu, HI, USA. [4] Earth System Modeling Center, Nanjing University of Science and Technology, Nanjing 210044, China. ✉email: hir.murakami@gmail.com

The locations and frequency of TC genesis (TCG) directly impact the TC track and landing locations, cumulative kinetic energy, and its impacts. Numerical modeling has been widely used to study the projected future changes in TCG frequency on the global scale[1–5]. Most previous studies project decreases in global TCG frequency[1–5]. Specifically, the projected decreases are more significant over the Southern Hemisphere, including the South Indian Ocean and South Pacific Ocean, than the Northern Hemisphere (see Fig. 5 and Table ES1 in Knutson et al.[2]). However, recent studies project future increases in the total global TCG frequency[6–9]. Therefore, projection of future changes in global TCG frequency remains highly uncertain with notable inter-model spread[2,3]. It is, therefore, critical to try to understand the physical reasons behind the projected changes.

Previous studies have proposed potential reasons for the projected future changes in global TCG frequency, such as changes in tropical overturning circulation associated with increased atmospheric static stability[10,11], entropy deficit[12], ventilation index[13], and frequency of cyclone seeds[8]. Although consensus has not been reached regarding the theory determining global TCG frequency and the projected future changes, it has been widely accepted that changes in TCG depends on the changes in the large-scale environmental conditions of the atmosphere and ocean. Thus, use of an empirical genesis potential index (GPI) that can depict such dynamic and thermodynamic conditions, such as the GPI developed by Emanuel and Nolan (hereafter ENGPI)[14], has been widely adopted as an approach to diagnosing the physical processes behind the projected future changes in TCG[15–20] as well as the observed intraseasonal, interannual, and interdecadal variability of TCG[21–24]. However, in the era spanning CMIP3 (phase 3 of the Coupled Model Inter-comparison Project)[17,18] to CMIP5 (i.e., phase 5 of CMIP)[20,25], the TCG frequency projected by models was often found to be inconsistent with that inferred by the ENGPI. Specifically, Camargo et al.[25] reported that GPIs that reproduces the TCG frequency well in the present-day climate do not always guarantee an equally successful reproduction of the projected future TCG frequency, posing a dilemma on the causes of future changes in TCG frequency.

The disparity between the TCG frequency projected by models and the TCG potential diagnosed by GPIs might exist because GPIs are optimized for the present-day climate and are not fully applicable in a warming climate[26,27]. In particular, the maximum potential intensity (MPI)—one of the thermodynamic factors of ENGPI—increases with rising sea surface temperatures (SSTs), and always leads to a projected increase in the ENGPI values[25]. On the other hand, dynamic variables have been found to be of primary importance for separating developing or non-developing disturbances in the western North Pacific under both the present-day and future warmer climate[26–28]. Some studies have also shown that the projected future changes in dynamic properties could be the main cause for the projected future changes in TCG frequency in the North Atlantic[29], Southwest Indian Ocean[30,31], and Australian region[32]. Specifically, a study on the projected future changes in TCG frequency in the South Indian Ocean showed future changes in ENGPI that were inconsistent with those in TCG frequency, but the dynamical elements in the ENGPI were better aligned than the thermodynamic elements with the projected changes in TCG frequency[30]. However, the relative importance of the dynamic factors versus the thermodynamic factors in diagnosing future changes in TCG frequency remains elusive[27]. Specifically, it is necessary to construct a new GPI that can represent both the present-day and future TCG climate to elucidate the potential physical mechanisms behind the future changes in TCG frequency.

Our developed dynamic GPI (DGPI), which contains four circulation factors, provides an alternative perspective for understanding the projected future changes in TCG frequency[27]. DGPI retains the two dynamic factors of ENGPI, i.e., the 850-hPa absolute vorticity and tropospheric vertical wind shear between 850 and 200 hPa, but the two thermodynamic factors of ENGPI, i.e., the MPI and 600-hPa relative humidity (RH_{600}), have been replaced by two new circulation factors: the vertical motion and meridional shear vorticity of the zonal winds at 500-hPa. Whilst the thermodynamic factors are not included in DGPI, they are by no means physically unimportant. In fact, the monthly mean RH_{600} is highly correlated with the 500-hPa vertical motion ($r = 0.84$, p-value < 0.01) over the domains of TCG, so the mid-tropospheric vertical motion, along with the vertical wind shear, can very well represent the effect of RH_{600}[27]. DGPI removes the MPI and implements the 500-hPa relative vorticity. The latter is important in the TCG activity of the Southern Hemisphere[27]. Besides, TC-permitting global model results have demonstrated that the four DGPI factors are the most influential in both present-day simulations and future projections under global warming[27].

Our group's previous study in which the newly developed DGPI was reported focused mainly on its skill in reproducing the TCG frequency in the present-day climate, but we have not yet published any results respect to future climate projections[27]. In this regard, the present study fills a knowledge gap in terms of the inconsistency between projected future changes in TCG and GPIs, and facilitates interpretation of the physical mechanisms behind the likely future changes in TCG frequency. Specifically, it is shown that DGPI projects a moderate decrease in TCG potential that is qualitatively more consistent with the TC-permitting and multimodel projections of CMIP5 and CMIP6 (Table 1 and S1, see the "Methods" section) relative to conventional GPIs such as ENGPI. We also aim in this paper to elaborate on the reasons for the projected changes in TCG frequency by identifying the contributions of individual GPI factors to TCG. The analysis of intermodal spread indicates that future changes in TCG frequency are principally controlled by the large-scale changes in vertical motion. On the other hand, the future change of MPI, which dominates the change in ENGPI, tends to project a conflicting pattern to TCG frequency projected by the models. The uncertainties associated with the thermodynamic factors are significantly larger than those associated the dynamic factors in explaining the projected changes in TCG frequency.

Results

Present-day TCG frequency represented by GPIs. In this study, the TCG frequency projected by the models is detected directly from the 6-hourly output with a metric of criteria including the maximum wind speed, warm core, minimum sea level pressure, low-level vorticity, and duration (see the "Methods" section).

The ENGPI[14] is defined as follows:

$$\mathrm{ENGPI} = (1.0 + 0.1\times V_s)^{-2.0}\left(\frac{\mathrm{dRH}_{600}}{50}\right)^3\left(\frac{\mathrm{MPI}}{70}\right)^3|\zeta_{a850}\times 10^5|^{1.5} \quad (1)$$

where RH_{600} (%) and MPI ($m\,s^{-1}$) are the thermodynamic factors. The MPI is determined by the vertical structure of temperature and moisture and SST[33]. Here, it is computed by using the formula given in Bester and Emanuel[34]. The dynamic factors, V_s and ζ_{a850}, represent the magnitude of the vertical wind shear ($m\,s^{-1}$) between 200 and 850 hPa and the absolute vorticity (s^{-1}) at 850 hPa, respectively.

The DGPI[27] consists of dynamic factors only, and the empirical formula is as follows:

$$\mathrm{DGPI} = (2.0 + 0.1\times V_s)^{-1.7}\left(5.5 - \frac{\mathrm{d}u_{500}}{\mathrm{d}y}\times 10^5\right)^{2.3} (5.0 - 20\times\omega_{500})^{3.4}(5.5 + |\zeta_{a850}\times 10^5|)^{2.4}\mathrm{e}^{-11.8} - 1.0 \quad (2)$$

where V_s and ζ_{a850} are the same as in Eq. (1), ω_{500} represents the

Table 1 List of CMIP6 models used in this study.

Model name	Expanded model name	Horizontal resolution [lat x lon]	TC detection criteria			Simulation used	
			ζ_{850} (m/s)	t_a (K)	d (h)	SSP2-4.5	SSP5-8.5
CMCC-CM2-SR5	Euro-Mediterranean Centre on Climate Change coupled climate model	1.25 × 0.9	8.500×10^{-5}	1.00	36		✓
CNRM_CM6-1-HR	Centre National de Recherches Meteorologiques Coupled Global Climate Model, version 6	0.5 × 0.5	1.400×10^{-4}	1.00	36		✓
MIROC6	Model for Interdisciplinary Research on Climate, version 6	1.4 × 1.4	1.125×10^{-4}	1.00	36	✓	✓
MPI-ESM1-2-HR	Max Planck Institute Earth System Model, medium resolution	0.9 × 0.9	1.0×10^{-5}	0.60	36	✓	✓
MRI-ESM2-0	Meteorological Research Institute Earth System Model 2.0	1.1 × 1.1	8.000×10^{-5}	1.00	36	✓	✓
NorESM2-MM	Norwegian Climate Center's Earth System Model	1.25 × 0.9	5.250×10^{-5}	1.00	36	✓	✓

The model-dependent criteria for TC detection are the relative vorticity at 850 hPa, temperature anomaly, and duration. The last column indicates the future scenarios used in this study.

vertical p-velocity (Pa s^{-1}) at 500 hPa, u_{500} denotes the zonal wind (m s^{-1}) at 500 hPa, and $-du_{500}/dy$ denotes the meridional shear vorticity associated with u_{500} (s^{-1}). Equation (2) is a more accurate version than the one used in Wang and Murakmai[27] and can be applied to 5° × 5° latitude–longitude grids to depict large-scale environmental conditions. A detailed description of the computation of DGPI as applied to reanalysis and model outputs is given in the "Methods" section.

The skill of the modified DGPI relative to ENGPI in representing the observed present-day TCG climatology and interannual variations is briefly evaluated in Fig. 1, and details for the original DGPI are available in Wang and Murakami[27]. Both DGPI and ENGPI realistically reproduce the observed spatial patterns of the annual mean TCG frequency (Fig. 1a–c). However, both indices significantly underestimate the maximum TCG frequency in the eastern and western North Pacific while slightly overestimating the TCG in the southwestern Pacific. For diagnosing interannual variations in TCG frequency in each ocean basin, ENGPI and DGPI have comparable skill in the North Atlantic and eastern Pacific, but DGPI shows improved skill in representing the interannual variations in TCG frequency in the western North Pacific and oceans of the Southern Hemisphere (Fig. 1d). Diagnosis of the TCG variability in the northern Indian Ocean remains a challenge. For the annual cycle of TCG frequency in each ocean basin, the two GPIs show comparable and reasonable skill, except in the North Indian Ocean (Fig. 1e).

Projected future changes in TCG frequency and distribution. How well do model-projected GPIs represent the model-projected TCG frequency and distribution? To address this question, we begin by examining a high-resolution TC-permitting model (namely, MRI-AGCM3.2S; see the "Methods" section, Fig. 2), followed by 19 CMIP5 and 6 CMIP6 coupled climate models (Fig. 3).

The TC-permitting model projects a future decrease in the total global number of TCGs by about −24.0%, with a general reduction within about 30° of latitude from the equator over the western North Pacific, South Indian Ocean, and South Pacific (Fig. 2i). In comparison, ENGPI projects an overall increase in most ocean basins, especially in the eastern North Pacific and South Indian Ocean. The total global value increases by about 14.0% (Fig. 2c), which is inconsistent overall with the changes in the model-projected TCG frequency (Fig. 2i). On the other hand, DGPI projects a decrease in the total global value (−6.1%, Fig. 2f) with significant decreases in the western Pacific that somewhat resemble the model-projected TCG changes. The spatial patterns of DGPI and the projected TCG frequency show a positive correlation ($r = +0.23$). In contrast, ENGPI and TCG frequency show no correlation ($r = -0.03$), suggesting that the spatial distribution of DGPI bears a relatively good resemblance to the projected TCG frequency, more so than ENGPI.

Forty future projections made with 19 CMIP5 and 6 CMIP6 models are examined (see the "Methods" section, Table 1 and S1), including 19 under the RCP 4.5 (medium emissions) scenario, 11 under the RCP8.5 (high emissions) scenario, 4 under the SSP2-4.5 (medium emissions) scenario, and 6 under the SSP5-8.5 (high emissions) scenario (Fig. 3). Under the RCP4.5 (RCP8.5) scenario, the ensemble average projects a moderate decrease in the total global TCG number by −2.9% (−10.0%) with an inter-model standard deviation of 13.6% (19.1%) (Fig. 3a, b). This result implies that the model-projected TCG frequency will likely (67% probability) range from −16.6% to +10.8% (−29.0% to +9.1%) under the RCP4.5 (RCP8.5) scenario. Note that the projected decrease is more significant with the increasing

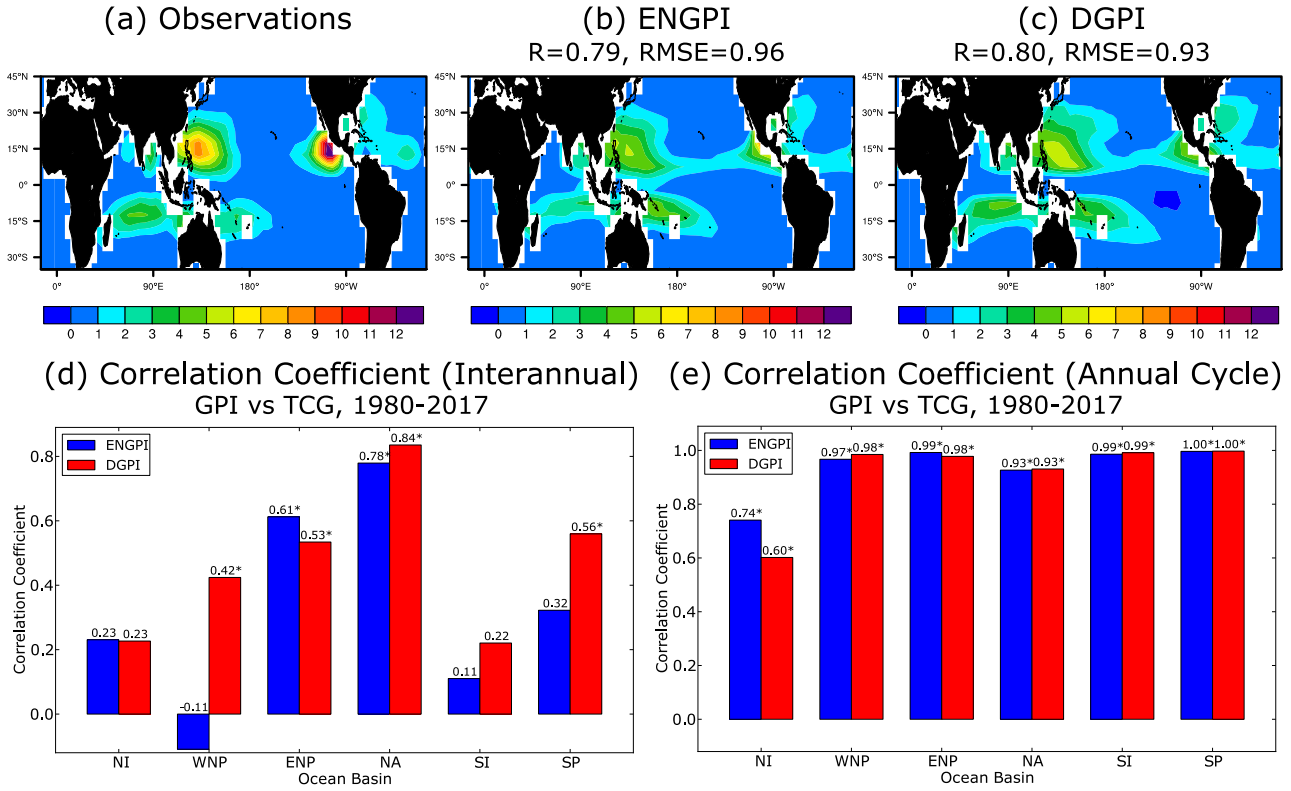

Fig. 1 Performance of ENGPI and DGPI in diagnosing the climatology, interannual, and seasonal variability of TCG frequency. The upper panels are the climatological annual mean TCG frequency in the observation (**a**) and the TCG potentials computed using ENGPI (**b**) and DGPI (**c**). Units are 0.1 × number per 5° × 5° grid cell per year. The spatial PCC and RMSE from the observed TCG frequency are shown at the top of the corresponding panels for ENGPI and DGPI. Panel (**d**) presents the interannual correlation coefficients between TCG frequency and the TCG potential computed by ENGPI (blue) and DGPI (red) in the six ocean basins: North Indian (NI); western North Pacific (WNP); eastern North Pacific (ENP); North Atlantic (NA); South Indian (SI); and South Pacific (SP). **e** As in (**d**), but for the 12-month climatological annual cycle. The ensemble mean dataset, derived from the five reanalysis datasets during 1980−2017, is used to compute the GPIs.

emissions from the mitigated (RCP4.5) scenario to the business-as-usual (RCP8.5) scenario. In contrast, the same model ensemble's ENGPI predicts a very likely (90% probability) increase in TCG potential under the RCP4.5 scenario. On the other hand, the ensemble DGPI predicts a moderate decrease in the TCG potential, corroborating the trend of the projected TCG frequency. Note that the DGPI-predicted TCG potential exhibits a substantially smaller intermodal spread (uncertainty) than the ENGPI-predicted TCG potential and the models' projected TCG frequency. The results from the CMIP6 models are generally consistent with those from the CMIP5 models (Fig. 3c, d). To reveal the consistency between the GPI and TCG changes, scatter plots of DGPI versus TCG as well as ENGPI versus TCG are presented in Fig. S1. The correlation coefficient between the ENGPI and TCG changes is −0.47, revealing that the future changes in ENGPI tend to be opposite in sign to those in TCG. Indeed, among the 40 simulations, only 8 (20%) of them show the projected future changes in ENGPI as having the same sign as those in TCG. Meanwhile, the correlation coefficient between the DGPI and TCG changes is low (−0.12), indicating that DGPI still fails to capture the changes in TCGs in quantitative terms. This means that a simulation with a larger decrease (or increase) in DGPI does not always show a larger decrease (or increase) in TCG, although there are 22 (55%) simulations that show the same sign of the change in DGPI and TCG.

Next, we examine how the GPI-predicted spatial pattern of TCG potential matches the projected TCG pattern for the individual CMIP5 and CMIP6 models (see Figs. S2–5 for the ensemble mean). The spatial pattern correlation coefficient (PCC) between the GPI-deduced TCG change (ΔGPI) and the projected TCG change (ΔTCG) measures their similarity in spatial distribution (Fig. 3e). For the multi-model ensemble mean, the PCC is +0.38 for DGPI and +0.08 for ENGPI. In nearly all experiments (39 out of the 40), compared with the ENGPI prediction, the DGPI-predicted pattern of change in TCG has higher PCCs with the TCG distribution. The root-mean-square error (RMSE) confirms that the DGPI-predicted pattern of change in TCG has overwhelmingly smaller errors than its ENGPI-predicted counterpart (Fig. 3f).

Primary factors controlling the future change in TCG frequency. Why do ENGPI and DGPI tend to project opposite future changes in GPI on a global scale? To address this question, we analyze each factor's contribution to the future changes in GPIs by using the following equation[35]:

$$\begin{aligned}\Delta\mathrm{GPI} =& \Delta F1 \cdot \overline{F2 \cdot F3 \cdot F4} + \Delta F2 \cdot \overline{F1 \cdot F3 \cdot F4} \\ &+ \Delta F3 \cdot \overline{F1 \cdot F2 \cdot F4} + \Delta F4 \cdot \overline{F1 \cdot F2 \cdot F3}\end{aligned} \quad (3)$$

where an overbar represents the present-day climatology and △ represents the projected future change. Each term on the right-hand side of Eq. (3) measures the fractional contribution of an individual factor to the total GPI change. The sum of the percentage contributions of all factors is equal to 100%. Although the contributions of some factors can exceed 100%, they might be canceled out by other factors with opposite contributions. Figure 4 shows the percentage contributions computed using the MRI-AGCM3.2S output data. Qualitatively similar results are also

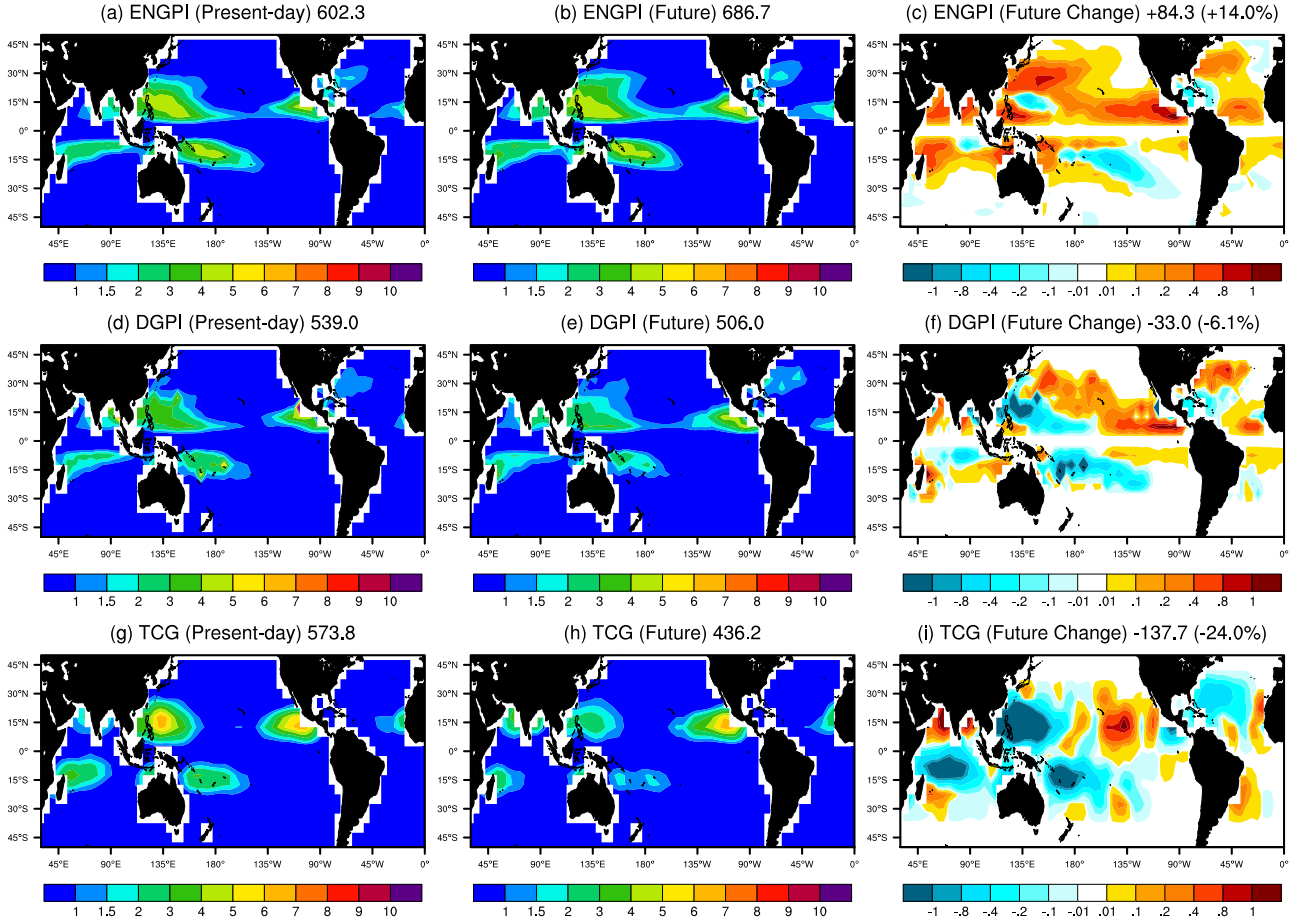

Fig. 2 Projected future changes in GPI and TCG frequency by MRI-AGCM3.2S. The results are from the 20-km resolution MRI-AGCM3.2 under the present-day climate (1979−2003) and high-emission RCP8.5 future scenario of CMIP5 (2075−2099): **a** ENGPI in the present-day simulation (1979−2003); **b** ENGPI in the future projection (2075−2099); **c** projected future changes in ENGPI. **d**–**f** As in **a**–**c** but for DGPI. **g**–**i** As in **a**–**c** but for the model-projected TCG frequency. The numbers in the titles indicate total TCG and GPIs, whereas the numbers in brackets indicate the fractional changes in future projections.

obtained using the ensemble mean of the CMIP5 models (Figs. S6, 7).

The dominant factor responsible for the decreasing DGPI is the mid-tropospheric vertical motion, ω_{500}; about 86% of changes is explained by the change in ω_{500} (Fig. 4b). The PCC between ω_{500} and DGPI is +0.84. These results indicate that ω_{500} determines the decreasing trend in DGPI in the western Pacific and North Atlantic and the increasing trend in the eastern Pacific. The mid-tropospheric shear vorticity and the 850-hPa absolute vorticity also contribute to the overall decreasing DGPI trend. However, the change in vertical wind shear increases the GPI and offsets the effect of the other three factors, resulting in a moderate decrease in the total TCG potential.

On the other hand, the dominant factor responsible for the increases in ENGPI is the MPI (Fig. 4g). The MPI increases everywhere owing to the projected increases in SST. The MPI contribution (+115%) dominates the total change in ENGPI. Also, the PCC between MPI and ENGPI is +0.62. However, the spatial pattern associated with the change in MPI (Fig. 4g) tends to be opposite to that associated with the projected change in TCG frequency (Fig. 2i), with a PCC of −0.58, suggesting that MPI provides an incorrect spatial distribution. The RH600 contributes to a decreasing ENGPI (Fig. 4i, −46%), while the wind shear favors an increasing ENGPI (Fig. 4h, +41%); thus, they offset each other in most places.

But which large-scale variable shows the most consistent spatial distribution to the projected TCG changes in the CMIP5 and CMIP6 models? To answer this, we evaluate the relationships between the GPI contribution from each element and the projected TCG frequency using the 30 CMIP5 and 10 CMIP6 model experiments (Fig. 5). We measure the relationship using the PCC between the projected pattern of changes in TCG and its counterpart inferred from the GPI due to a change in an individual factor. The latter computes the partial change in the GPI by varying a specific factor [i.e., Eq. (3)]. A positive correlation means that the change in the spatial pattern of the GPI due to a particular factor generally agrees with the model-projected TCG frequency pattern. A negative correlation means the opposite. The intermodel spread measures the associated uncertainty.

The results for the DGPI projection by the 30 CMIP5 experiments indicate that the changes in the low-level absolute vorticity and mid-tropospheric vertical motion very likely have a robust positive relationship with the projected TCG change (Fig. 5a). The spatial pattern of the changes in the vertical wind shear and mid-tropospheric vorticity are moderately consistent with that of the changes in TCG frequency, albeit with large uncertainties, and thus we consider their contribution to be uncertain. The model results for ENGPI projection confirm the robust linkage between the low-level absolute vorticity and TCG changes and the

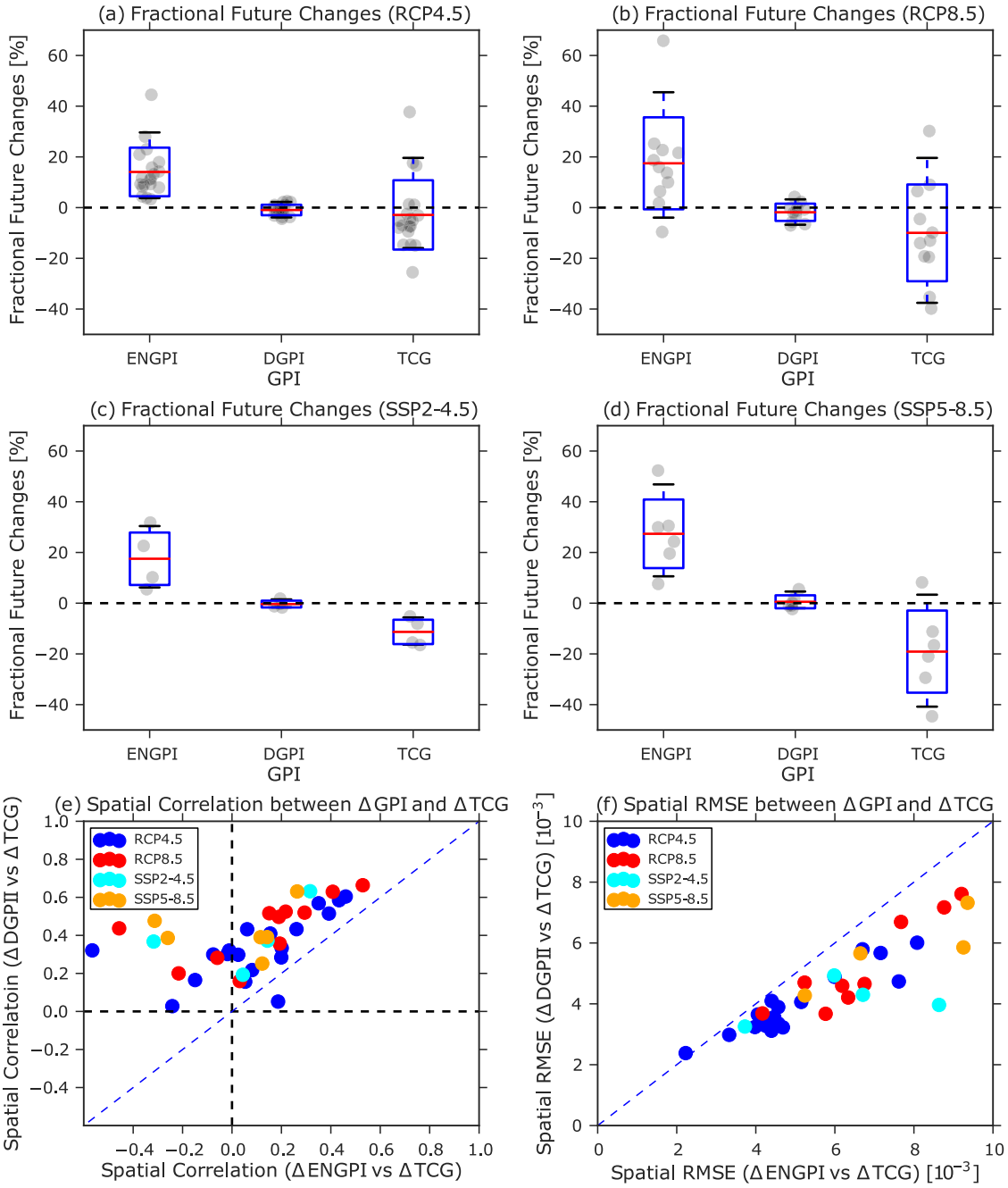

Fig. 3 Projected future changes in GPI and detected TCG frequency. The analyzed domain is in the tropics (30°S–30°N) using the 19 CMIP5 models (19 models under RCP4.5 and 11 models under RCP8.5) and 6 CMIP6 models (4 models under SSP2-4.5 and 6 models under SSP5-8.5). The future change is determined by the reference between the future projection (2075–2099) and the historical simulations (1979–2003). **a** Box plot for future changes in GPI and TCG for RCP4.5. The boxes represent the range of the mean plus or minus one standard deviation of the intermodal spread in units of percentage changes, which represents the "likely" change. The horizontal red lines show the mean values, and the dashed bars show the 5% and 95% quantiles, representing the range of "very likely" change. **b**–**d** As in **a**, but for RCP8.5, SSP2-4.5, and SSP5-8.5 scenario, respectively. **e** Spatial PCCs between the future changes in ENGPI and TCG frequency (*x*-axis) compared with those between DGPI and TCG frequency (*y*-axis). The dots above the blue dashed diagonal line indicate that the spatial pattern of the changes in DGPI is closer to those in TCG than that in ENGPI. **f** As in **e**, but for RMSE. The dots below the blue dashed diagonal line indicate that the mean errors of DGPI are smaller than those of ENGPI in representing the TCG frequency.

uncertain relationship between the vertical wind shear and TCG changes (Fig. 5b). Notably, the MPI likely has a significant negative correlation with the projected pattern of change in TCG. The reason is that MPI increases with rising SST and projects a significant increase in genesis potential under global warming (Fig. 4g). However, the threshold SST value for TCG in a warming world will also increase[36,37]; thus, the MPI derived from the present-day climate is not appropriate for diagnosing future changes in TCG. Besides, the relationships between the thermodynamic factor (RH_{600}) and TCG changes in ENGPI show considerably larger uncertainties than the corresponding dynamic factor (mid-tropospheric vertical motion). Consistent results were also obtained using the 10 CMIP6 experiments (Fig. 5c, d).

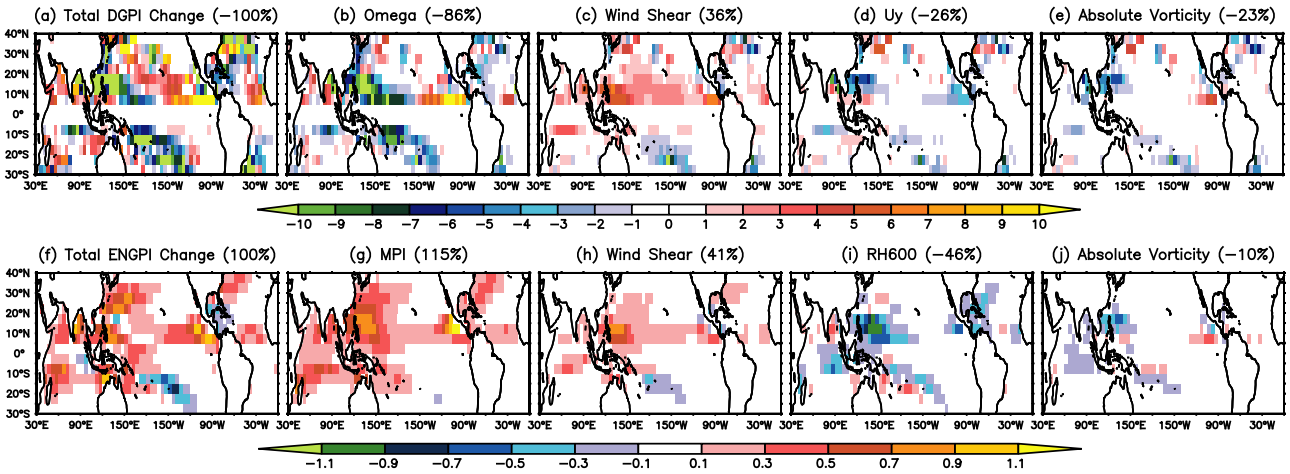

Fig. 4 Fractional contribution of each factor to the future changes in the total GPI. The fractional contribution was determined using the output from MRI-AGCM under the RCP8.5 scenario. **a** Total changes in DGPI, and the contribution to the total DGPI change from each factor: **b** 500-hPa vertical motion, **c** vertical wind shear, **d** 500-hPa shear vorticity of zonal wind, U_y, and **e** 850-hPa absolute vorticity. **f**–**j** As in **a**–**e** but for ENGPI. Each term's contribution to the total ENGPI change is shown for **g** MPI, **h** vertical wind shear, **i** RH_{600}, and **j** 850-hPa absolute vorticity. The numbers in brackets indicate the fractional contribution by each factor to the total GPI changes. Because the global-total GPI change is negative for DGPI (**a**–**e**), the sign of the total GPI change is reversed (i.e., −100%).

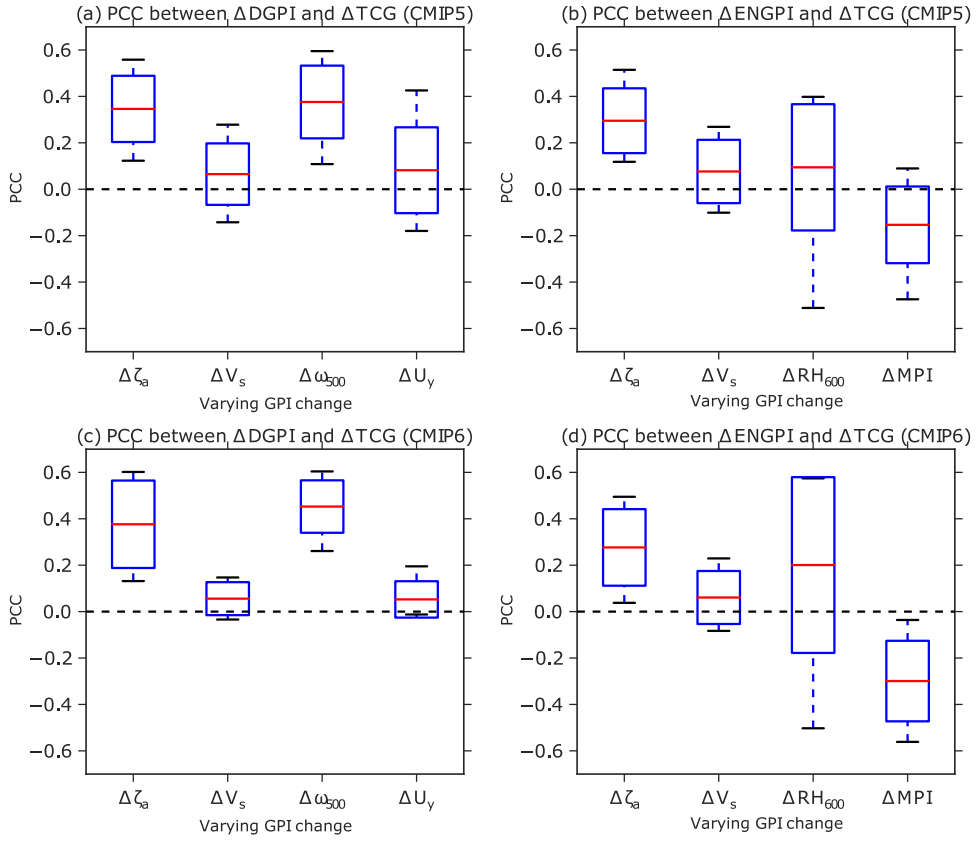

Fig. 5 Spatial PCC between each GPI factor's contribution and the projected TCG frequency. a DGPI and **b** ENGPI using the 30 CMIP5 model experiments under the RCP4.5 and RCP8.5 scenarios. **c** and **d** As in **a** and **b**, but for the 10 CMIP6 model experiments under the SSP2-4.5 and SSP5-8.5 scenarios. The box plots show the PCC between the changes in TCG frequency and the changes in GPI by varying a single factor. The abscissa in **a**, **c** denotes DGPI changes by varying absolute vorticity ($\Delta\zeta_a$), vertical wind shear (ΔV_s), vertical motion ($\Delta\omega_{500}$), and mid-level vorticity (ΔU_y), respectively. The abscissa in **b**, **d** denotes ENGPI changes by varying absolute vorticity ($\Delta\zeta_a$), vertical wind shear (ΔV_s), RH (ΔRH_{600}), and MPI (ΔMPI), respectively. The boxes represent the range of one standard deviation of the correlations; the horizontal red lines show the mean value, and the dashed bars show the 5% and 95% quantiles.

Summary and discussion

ENGPI and DGPI possess comparable skill in diagnosing the present-day climatology, as well as the annual and seasonal variability of TCG frequency (Fig. 1). However, ENGPI projects a significant increase in TCG potential in CMIP5 and CMIP6 models, while DGPI projects a moderate decrease or no change (Fig. 3). Relative to ENGPI, DGPI shows total future changes that are more consistent with the changes in TCG produced by the TC-permitting model (MRI AGCM3.2S; Fig. 2) and most low-resolution CMIP5 and CMIP6 models (Fig. 3a–d). The projected changes in DGPI show significantly better agreement than those in ENGPI with the spatial pattern of the projected changes in TCG (Fig. 3e, f).

The inconsistency between the projected changes in ENGPI and TCG frequency lies in the dominant contribution of the thermodynamic factor, MPI, to ENGPI. The spatial pattern of the genesis potential arising from the change in MPI contradicts the model-projected changes in TCG distribution (Figs. 4 and 5). The moderate decreasing trend of TCG projected by DGPI is primarily attributable to future weakening of the mid-tropospheric upward motion (Fig. 4). The spatial pattern of the changes in DGPI due to 500-hPa ascending motion is significantly and positively correlated to the projected change in TCG frequency distribution in the CMIP 5 and CMIP6 models (Fig. 5), confirming the robust correlation between vertical motion and the changes in TCG as reported in previous studies[10,11]. Besides, the low-level absolute vorticity and mid-tropospheric vorticity also contribute to the decreasing DGPI, while the reduced reduction in vertical wind shear tends to increase DGPI.

We argue that greenhouse gas (GHG) radiative forcing-induced horizontally differential heating drives the circulation changes, shaping future changes in TCG. The differential heating is associated with the robust "warmer Northern Hemisphere than Southern Hemisphere" and "warmer land than ocean" patterns, as well as the uncertain tropical SST patterns (e.g., El Niño-like warming)[38]. However, GHG-induced vertically differential (top-heavy) heating stabilizes the atmosphere and affects the circulation conditions. The stabilization of the atmosphere suppresses the mid-tropospheric ascending motion (thus reducing the RH_{600}) and vertical wind shear. The importance of mid-tropospheric vertical motion is in line with a hypothesis proposed by previous studies[10,11] in which projected weakening of the tropical overturning circulation (e.g., weakening of the Hadley or Walker circulations) should be the main reason for the projected decreases in TCG. In general, mean upward motion is important for TCG because the boundary layer flows converge and the upward transfer of moisture increases the mid-level RH. Both the dynamic and thermodynamic conditions are also conducive to initiation of organized convection or incipient cyclonic circulation (i.e., "seeds").

The TC-permitting model results suggest that weakening of the mid-tropospheric ascending motion decreases the genesis potential, while reduced vertical shear increases the genesis potential (Fig. 4). As a result of this cancellation, the overall decrease in the TCG potential is moderate. However, in the CMIP5 and CMIP6 models, the vertical shear-induced GPI change is weakly related to the projected TCG change, casting doubt on the role of vertical wind shear as suggested by the TC-permitting model. This issue warrants further in-depth investigation. In general, given the significant uncertainties in the CMIP5 models, the mechanisms responsible for the future changes in TCG deserve further investigation using CMIP6 models. Although the availability of 6-hourly data is limited for the CMIP6 models, we were able to confirm that the results using the 6 CMIP6 models employed in this study are consistent overall with the CMIP5 models.

Finally, we preliminarily investigated another GPI formula proposed by Tippett et al.[39] and found that his GPI shows similar skill to ENGPI for the interannual variation and annual cycle in the present climate (Fig. S8). The projected future changes in Tippett et al.'s GPI tend to show increases in the total global values (Fig. S9). In addition, we can confirm that consistent results can be obtained when the analysis is applied to the peak storm season (May–October for the Northern Hemisphere and November–April for the Southern Hemisphere) instead of all seasons (January–December) (Fig. S10 for example).

Methods

Observational data. The observed TCG frequency was determined based on IBTrACS, version v04r00[40], over 1980–2017. We utilized the National Hurricane Center and the Joint Typhoon Warning Center in the IBTrACS dataset. Observed SSTs over the same period were obtained from the UK Met Office Hadley Centre SST product (HadISST1.1)[41]. Atmospheric large-scale variables were obtained from the ensemble mean (equal-weighted average) of five reanalysis datasets over 1980–2017 to minimize the uncertainty in the individual reanalysis datasets. They were: ECMWF's Interim Reanalysis (ERA-Interim)[42]; NCEP's Climate Forecast System Reanalysis (CFSR)[43]; NASA's Modern-Era Retrospective Analysis for Research and Applications, version 2 (MERRA-2)[44]; NCEP/NCAR Reanalysis II (NCEP-2)[45]; and the Japanese 55-year reanalysis (JRA-55)[46].

Models. We first applied DGPI and ENGPI to the monthly model outputs using the 20-km-mesh Meteorological Research Institute (MRI) Atmospheric General Circulation Model (AGCM) version 3.2 (MRI-AGCM3.2S)[47,48]. MRI-AGCM3.2S reasonably reproduces the observed intense TCs of Category 4 and 5 and the global TC distribution[48]. Two 25-yr experiments were utilized for the present-day (1979–2003) and the projected future warmer climate (2075–2099). The future projection was conducted based on the IPCC's RCP8.5 scenario[47,48]. The future changes in SST were estimated from the ensemble mean of 28 models that participated CMIP5 under the RCP8.5 scenario[49,50].

We also utilized 19 CMIP5 and 6 CMIP6 models (Table 1 and S1). Unlike MRI-AGCM3.2S, the horizontal resolution of the CMIP5 and CMIP6 models ranges from 0.5° to 2.8°, and this low horizontal resolution makes it difficult to resolve TCs. However, some CMIP5 models show reasonable TC-like vortexes in their present-day simulations[51]. Projection results used in Murakami et al.[51] under the present-day climate (1979–2003) and future RCP4.5 and RCP8.5 scenarios (2075–2099) were used in this study for the CMIP5 models. The same analysis was repeated with the CMIP6 models, although only 6 CMIP6 models were analyzed in this study owing to the limited availability of 6-hourly data needed for TC detection. Among the several ensemble members in the present-day and future simulations by the CMIP5 and CMIP6 models, only one ensemble member for each model was used.

TC detection methods. Model-simulated TCs were detected directly from the 6-hourly output by the following model-dependent and globally uniform criteria reported in Murakami et al.[51] and Murakami and Sugi[52]. In short, three criteria are considered: relative vorticity at 850 hPa (ζ_{850}), the temperature anomaly in the warm core region (t_a), and the duration that satisfies ζ_{850} and t_a (d). The model-dependent criteria are optimized for a given model configuration to ensure that the present-day global mean TC number matches the observed values (84 per year). The applied criteria (i.e., ζ_{850}, t_a, and d) are listed in Table S1 for each CMIP5 model and Table 1 for each CMIP6 model. The positions of TCG (first points of TC tracks) were counted within the global domain at 6-hourly intervals in each 5° × 5° grid box. The total count for each grid box is defined as the TCG frequency.

DGPI. The DGPI formula used in this study [i.e., Eq. (3)] is a modified version of the DGPI that was originally proposed by Wang and Murakami[27]. The modified DGPI values were computed over a 5° × 5° grid box in this study. First, we computed DGPI values for each month, and then averaged them for calculating the climatological mean values. Wang and Murakami[27] showed that there no TCG occurs over the domain of 5°S–5°N or in the region where the relative SST anomaly ($RSST_a$) is lower than zero for both observations and the model simulations. Therefore, following Wang and Murakami[27], we replaced the computed DGPI values with zero over the domains of 5°S–5°N or $RSST_a < 0$. Here, RSSTa is defined as the anomaly of local SST relative to the tropical (30°S–30°N) mean SST.

Data availability

The observed TC data (IBTrACS) are publicly available at https://www.ncdc.noaa.gov/ibtracs/. The observed SST data (HadISST1.1) are available at https://www.metoffice.gov.uk/hadobs/hadisst/. The reanalysis datasets are available at https://apps.ecmwf.int/datasets/data/interim-full-moda/levtype=sfc/ for ERA-Interm; https://climatedataguide.ucar.edu/climate-data/climate-forecast-system-reanalysis-cfsr for CFSR; https://disc.gsfc.nasa.gov/datasets?project=MERRA-2 for MERRA-2; https://psl.noaa.gov/data/gridded/

data.ncep.reanalysis2.html for NCEP2; and https://jra.kishou.go.jp/JRA-55/index_en.html for JRA55. The model outputs by MRI-AGCM are online available at http://search.diasjp.net/en/dataset/GCM20_SOUSEI. The datasets and codes generated during and/or analyzed during the current study are available in https://doi.org/10.7910/DVN/PDJ34K. These uploaded files are freely available.

Code availability

The Python codes to compute DGPI and ENGPI are provided in https://doi.org/10.7910/DVN/PDJ34K. These uploaded codes are freely available for any purpose.

Received: 1 November 2021; Accepted: 9 March 2022;
Published online: 01 April 2022

References

1. Knutson, T. et al. Tropical cyclones and climate change. *Nat. Geosci.* **3**, 157–163 (2010).
2. Knutson, T. et al. Tropical cyclones and climate change assessment: Part II. Projected response to anthropogenic warming. *Bull. Am. Meteor. Soc.* **101**, E303–E322 (2020).
3. IPCC. Climate change 2013: the physical science basis. In *Contribution of Working Group I to the Fifth Assessment Report of the Intergovern-mental Panel on Climate Change* (eds Stocker, T. F., Qin, D., Plattner, G. -K., Tignor, M., Allen, S. K., J. Boschung, J., Nauels, A., Xia, Y., Bex, V. & Midgley, P. M.) 1535 (Cambridge University Press, Cambridge, UK and New York, NY, USA, 2013).
4. Walsh, K. et al. Hurricanes and climate: the US CLIVAR working group on hurricanes. *Bull. Am. Meteorol. Soc.* **96**, 997–1017 (2015).
5. Walsh, K. J. E. et al. Tropical cyclones and climate change. *Trop. Cyclone Res. Rev.* **8**, 240–250 (2019).
6. Emanuel, K. Increased global tropical cyclone activity from global warming: results of downscaling CMIP5 climate models. *Proc. Natl Acad. Sci. USA* **110**, 12219–12224 (2013).
7. Bhatia, K. T., Vecchi, G. A., Murakami, H., Underwood, S. & Kossin, J. Projected response of tropical cyclone intensity and intensification in a global climate model. *J. Clim.* **31**, 828–8303 (2018).
8. Vecchi, G. A. et al. Tropical cyclone sensitivities to CO_2 doubling: roles of atmospheric resolution, synoptic variability and background climate changes. *Clim. Dyn.* **53**, 5999–6033 (2019).
9. Emanuel, K. Response of global tropical cyclone activity to increasing CO_2: Results from downscaling CMIP6 models. *J. Clim.* **34**, 75–70 (2021).
10. Bengtsson, L., Botzet, M. & Esch, M. Will greenhouse gas-induced warming over the next 50 years lead to higher frequency and greater intensity of hurricanes? *Tellus* **48A**, 57–73 (1996).
11. Sugi, M., Noda, A. & Sato, N. Influence of the global warming on tropical cyclone climatology. *J. Meteor. Soc. Jpn.* **80**, 249–272 (2002).
12. Emanuel, K., Sundararajan, R. & Williams, J. Hurricanes and global warming: results from downscaling IPCC AR4 simulations. *Bull. Am. Meteor. Soc.* **89**, 347–367 (2008).
13. Tang, B. & Camargo, S. J. Environmental control of tropical cyclones in CMIP5: a ventilation perspective. *J. Adv. Model. Earth Syst.* **6**, 115–128 (2014).
14. Emanuel, K. A. & Nolan, D. S. Tropical cyclone activity and global climate. *Proc. 26th Conference on Hurricanes and Tropical Meteorology* 240–241. (American Meteorological Society, Miami, FL, 2004). Preprints.
15. Gualdi, S., Scoccimarro, E. & Navarra, A. Changes in tropical cyclone activity due to global warming: results from a high-resolution coupled general circulation model. *J. Clim.* **21**, 5204–5228 (2008).
16. Yokoi, S. & Takayabu, Y. N. Multi-model projection of global warming impact on tropical cyclone genesis frequency over the western North Pacific. *J. Meteor. Soc. Jpn.* **87**, 525–538 (2009).
17. Yamada, Y., Oouchi, K., Satoh, M., Tomita, H. & Yanase, W. Projection of changes in tropical cyclone activity and cloud height due to greenhouse warming: global cloud-system-resolving approach. *Geophys. Res. Lett.* **37**, L07709 (2010).
18. Murakami, H. & Wang, B. Future change of North Atlantic tropical cyclone tracks: projection by a 20-km-mesh global atmospheric model. *J. Clim.* **23**, 2699–2721 (2010).
19. Murakami, H., Wang, B. & Kitoh, A. Future change of western North Pacific typhoons: projections by a 20-km-mesh global atmospheric model. *J. Clim.* **24**, 1154–1169 (2011).
20. Yokoi, S., Takahashi, C., Yasunaga, K. & Shirooka, R. Multi-model projection of tropical cyclone genesis frequency over the western North Pacific: CMIP5 results. *SOLA* **8**, 137–140 (2012).
21. Camargo, S. J., Wheeler, M. C. & Sobel, A. H. Diagnosis of the MJO modulation of tropical cyclogenesis using an empirical index. *J. Atmos. Sci.* **66**, 3061–3074 (2009).
22. Camargo, S. J., Emanuel, K. A. & Sobel, A. H. Use of a genesis potential index to diagnose ENSO effects on tropical cyclone genesis. *J. Clim.* **20**, 4819–4834 (2007).
23. Watterson, I. G., Evans, J. L. & Ryan, B. F. Seasonal and interannual variability of tropical cyclogenesis: diagnostics from large-scale fields. *J. Clim.* **8**, 3052–3066 (1995).
24. Goldenberg, B., Landsea, C. W., Mestas-Nuñez, A. M. & Gray, W. M. The recent increase in Atlantic hurricane activity: causes and implications. *Science* **293**, 474–479 (2001).
25. Camargo, S., Tippett, M. K., Sobel, A. H., Vecchi, G. A. & Zhao, M. Testing the performance of tropical cyclone genesis indices in future climates using the HiRAM model. *J. Clim.* **27**, 9171–9196 (2014).
26. Murakami, H., Li, T. & Peng, M. Changes to environmental parameters that control tropical cyclone genesis under global warming. *Geophys. Res. Lett.* **40**, 2265–2270 (2013).
27. Wang, B. & Murakami, H. Dynamic genesis potential index for diagnosing present-day and future global tropical cyclone genesis. *Environ. Res. Lett.* **15**, 114008 (2020).
28. Fu, B., Peng, M. S. & Li, T. Developing versus nondeveloping disturbances for tropical cyclone formation. Part II: Western North Pacific. *Mon. Weather Rev.* **140**, 1067–1080 (2012).
29. Chauvin, F., Pilon, R., Palany, P. & Belmadani, A. Future changes in Atlantic hurricanes with the rotated-stretched ARPEGE-Climat at very high resolution. *Clim. Dyn.* **54**, 947–972 (2020).
30. Malherbe, J., Engelbrecht, F. A. & Landman, W. A. Projected changes in tropical cyclone climatology and landfall in the Southwest Indian Ocean region under enhanced anthropogenic forcing. *Clim. Dyn.* **40**, 2867–2886 (2013).
31. Cattiaux, J., Chavin, F., Bousquet, O., Malardel, S. & Tsai, C.-L. Projected changes in the Southern Indian Ocean cyclone activity assessed from high-resolution experiments and CMIP5 models. *J. Clim.* **33**, 4975–4991 (2020).
32. Lavender, S. L. & Walsh, K. J. E. Dynamically downscaled simulations of Australian region tropical cyclones in current and future climates. *Geophys. Res. Lett.* **38**, L10705 (2011).
33. Emanuel, K. A. Sensitivity of tropical cyclones to surface exchange coefficients and a revised steady-state model incorporating eye dynamics. *J. Atmos. Sci.* **52**, 3969–3976 (1995).
34. Bister, M. & Emanuel, K. A. Dissipative heating and hurricane intensity. *Meteor. Atmos. Phys.* **52**, 233–240 (1998).
35. Li, Z., Yu, W., Li, T., Murty, V. S. N. & Tangang, F. Bimodal character of cyclone climatology in the Bay of Bengal modulated by Monsoon seasonal cycle. *J. Clim.* **26**, 1033–1046 (2013).
36. Wehner, M., Prabhat, K. A. R., Stone, D., Collins, W. D. & Bacmeister, J. Resolution dependence of future tropical cyclone projections of CAM5.1 in the U.S. CLIVAR hurricane working group idealized configurations. *J. Clim.* **28**, 3905–3925 (2015).
37. Sugi, M., Yoshida, K. & Murakami, H. More tropical cyclones in a cooler climate. *Geophys. Res. Lett.* **42**, 6780–6784 (2015).
38. Wang, B., Jin, C. & Liu, J. Understanding future change of global monsoon projected by CMIP6 models. *J. Clim.* **33**, 6471–6489 (2020).
39. Tippett, M. K., Camargo, S. J. & Sobel, A. H. A Poisson regression index for tropical cyclone genesis and the role of large-scale vorticity in genesis. *J. Clim.* **24**, 2335–2357 (2011).
40. Knapp, K. R., Kruk, M. C., Levinson, D. H., Diamond, H. J. & Neumann, C. J. The international best track archive for climate stewardship (IBTrACS): unifying tropical cyclone best track data. *Bull. Am. Meteor. Soc.* **91**, 363–376 (2010).
41. Rayner, N. A. et al. Global analysis of sea surface temperature, sea ice, and night marine air temperature since the late nineteenth century. *J. Geophys. Res.* **108**, 4407 (2003).
42. Dee, D. P. et al. The ERA-Interim re-analysis: configuration and performance of the data assimilation system. *Q. J. R. Meteorol. Soc.* **137**, 553–597 (2011).
43. Saha, S. et al. The NCEP climate forecast system reanalysis. *Bull. Am. Meteor. Soc.* **91**, 1015–1057 (2010).
44. Reichle, R. et al. Land Surface Precipitation in MERRA-2. *J. Clim.* **30**, 1643-–11664 (2017).
45. Kanamitsu, M. et al. NCEP-DOE AMIP-II reanalysis (R-2). *Bull. Am. Meteor. Soc.* **83**, 1631–1643 (2002).
46. Kobayashi, S. et al. The JRA-55 reanalysis: general specifications and basic characteristics. *J. Meteor. Soc. Jpn.* **93**, 5–48 (2015).
47. Mizuta, R. et al. Climate simulations using MRI-AGCM3.2 with 20-km grid. *J. Meteor. Soc. Jpn.* **90A**, 233–258 (2012).
48. Murakami, H. et al. Future changes in tropical cyclone activity projected by the new high-resolution MRI-AGCM. *J. Clim.* **25**, 3237–3260 (2012).
49. Christensen, J. H. et al. Climate phenomena and their relevance for future regional climate change. In *Climate Change 2013: The physical science basis. Contribution of Working Group I to the Fifth Assessment Report of the Intergovernmental Panel on Climate Change* (eds Stocker, T. F., Qin, D., Plattner, G.-K., Tignor, M., Allen, S. K., Boschung, J., Nauels, A., Xia, Y., Bex, V. & Midgley, P. M.) 1217–1308 (Cambridge University Press, Cambridge, UK; New York, NY, 2013).

50. Taylor, K. E., Stouffer, R. J. & Meehl, G. A. An overview of CMIP5 and the experiment design. *Bull. Am. Meteor. Soc.* **93**, 485–498 (2012).
51. Murakami, H., Hsu, P.-C., Arakawa, O. & Li, T. Influence of model biases on projected future changes in tropical cyclone frequency of occurrence. *J. Clim.* **27**, 2159–2181 (2014).
52. Murakami, H. & Sugi, M. Effect of model resolution on tropical cyclone climate projections. *SOLA* **6**, 73–76 (2010).

Acknowledgements

BW is supported by the National Science Foundation (Climate Dynamics Division) Award # 2025057. This paper is IPRC publication #1560, SOEST publication # 11491, and ESMC publication #376. We appreciate the three anonymous reviewers for thoughtful comments on this study.

Author contributions

H.M. analyzed the data and drafted the manuscript. B.W designed the study and drafted the manuscript.

Competing interests

The authors declare no competing interests.

Additional information

Supplementary information The online version contains supplementary material available at https://doi.org/10.1038/s43247-022-00410-z.

Correspondence and requests for materials should be addressed to Hiroyuki Murakami.

Peer review information *Communications Earth & Environment* thanks the anonymous reviewers for their contribution to the peer review of this work. Primary Handling Editors: [EBM name(s)] and [Internal Editor name(s)]. Peer reviewer reports are available.